Fundamental gain in high-contrast imaging with the large binocular telescope interferometer

Patru, Fabien, Esposito, Simone, Puglisi, Alfio, Riccardi, Armando, Pinna, Enrico, et al.

Fabien Patru, Simone Esposito, Alfio Puglisi, Armando Riccardi, Enrico Pinna, Carmelo Arcidiacono, John Hill, Philip Hinz, "Fundamental gain in high-contrast imaging with the large binocular telescope interferometer," Proc. SPIE 9907, Optical and Infrared Interferometry and Imaging V, 99071S (4 August 2016); doi: 10.1117/12.2232061

SPIE.

Event: SPIE Astronomical Telescopes + Instrumentation, 2016, Edinburgh, United Kingdom

Fundamental gain in high contrast imaging with the Large Binocular Telescope Interferometer

Fabien Patru[a], Simone Esposito[a], Alfio Puglisi[a], Armando Riccardi[a], Enrico Pinna[a], Carmelo Arcidiacono[a], John Hill[b], Philip Hinz[b]

[a] Osservatorio Astrofisico di Arcetri, 5 Largo Enrico Fermi, 50125, Firenze, Italia
[b] LBT Observatory, 933 N. Cherry Ave, AZ 85721, Tucson, United States

ABSTRACT

Numerical simulations for the Large Binocular Telescope Interferometer have shown a fundamental gain in contrast when using two $8m$ adaptive optics telescopes instead of one, assuming a high Strehl and a cophasing mode. The global gain is improved by a factor 2 in contrast by using the long exposures and by a factor of 10 in contrast by using the short exposures. Indeed, fringes are still present in the short exposure, contrary to the long exposure where the fringes are blurred. Thus, there is some gain in grouping some short exposures with high gain G. This makes the LBTI well suitable for the Angular Differential Imaging technique. A planet will be alternatively located in the dark fringes ($G \approx 10$ to 100) and/or in the dark rings ($G \approx 4$ to 20). A rotation of 15° is sufficient to pass through at least one gain zone. The LBTI can provide in the visible wavelengths not only high angular resolution ($\approx 6.5mas$ at $750nm$) and high sensitivity (by a factor 4), but also a gain in contrast (by a factor 10 to 100) compared to the stand-alone adaptive optics used on each LBT aperture.

Keywords: Large Binocular Telescope Interferometer, interferometry, adaptive optic, point spread function, dynamic range, high contrast imaging angular differential imaging

1. INTRODUCTION

The LBTI (Large Binocular Telescope Interferometer) in Arizona can be used as an image-plane Fizeau interferometer, combining the beams from the two $8m$ primary mirrors of the LBT (Large Binocular Telescope) (1; 2). Preserving the phase information would allow true imaging over the field of view corrected by each single adaptive optics (AO) system. The first light adaptive optics (FLAO) have been used efficiently at the LBT by means of a pyramid wavefront sensor (3). First fringes were achieved in 2010, dual-aperture AO-corrected fringes in 2012 (4; 5), and first closed-loop observations with path length stabilization in 2013 (6). The LBTI can deliver the sensitivity of a $12m$ telescope and the spatial resolution of a $23m$ telescope, over a wide field of view of the order of few arcseconds square (7). We show in this paper that the LBTI can also offer a significant gain in contrast, by properly combining the two separated wavefronts from each sub-aperture.

The study presented here has been initiated in the framework of the project LIVE (LBT Interferometer Visible Experiment) (8) proposed to the LBTO comity as a visible mode at the LBTI for exoplanets imaging. Providing a given phase power spectral density of the atmosphere compensated by AO, a temporal sequence of frames is generated by a home-made simulation tool developed in INAF-Arcetri. Errors are introduced to reproduce realistic wavefronts corrected by a FLAO system and injected into the LBTI beam combiner. Those numerical simulations provide results in agreement with simulations using FLAO on-sky data (9). Our study has been restrained to monochromatic light in the visible wavelengths ($\lambda = 750nm$). These results can be easily transposed into other wavelengths.

Further author information: (Send correspondence to Fabien Patru and Simone Esposito)
Fabien Patru: E-mail: fabienpatru@gmail.com
Simone Esposito: E-mail: esposito@arcetri.astro.it

Optical and Infrared Interferometry and Imaging V, edited by Fabien Malbet, Michelle J. Creech-Eakman, Peter G. Tuthill, Proc. of SPIE Vol. 9907, 99071S
 · doi: 10.1117/12.2232061

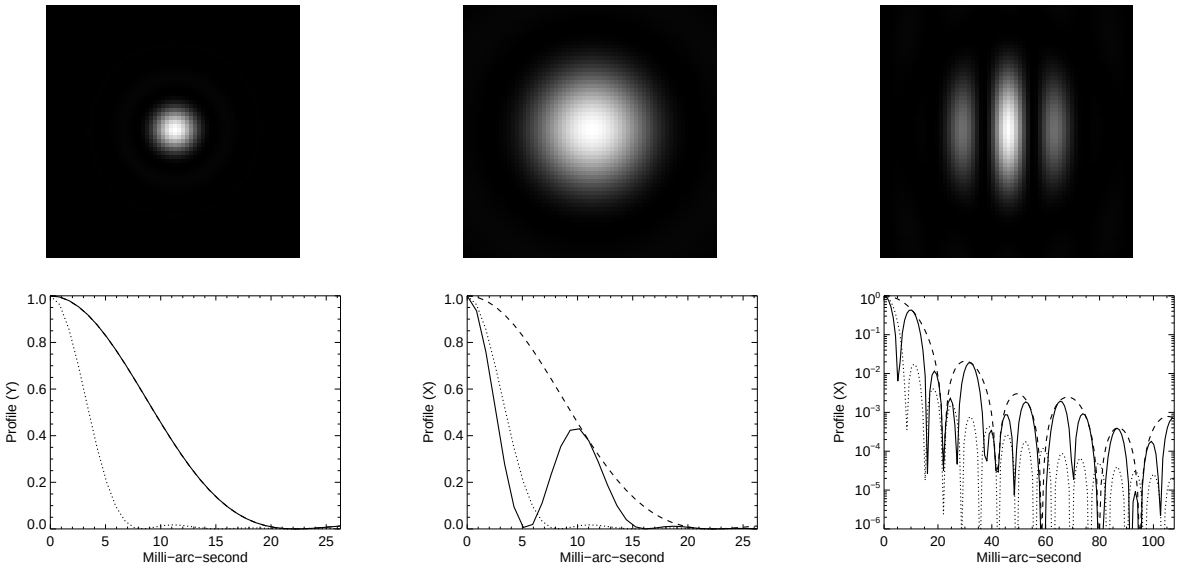

Figure 1. Theoretical PSF in a focal plane. PSF distributions with a linear scale (top) of a $23m$ telescope (left), an $8m$ LBT telescope (middle) and the LBTI interferometer (right). PSF profiles (bottom) of a $23m$ telescope (dotted line), an $8m$ LBT telescope (dashed line) and the LBTI interferometer (solid line) in the Y direction perpendicular to the LBTI baseline (left) and in the X direction parallal to the LBTI baseline (middle and right). The fringes appears within an Airy envelope, due to the double-aperture nature of the LBTI. The PSF with a logarithmic scale (bottom right) shows that the theoretical contrast of the LBTI is better than the contrast achieved by a single $8m$ LBT telescope and decreases down to the same level of a $23m$ telescope in some areas of the PSF.

We compare the Point Spread Function (PSF) of an LBT aperture and of the LBTI interferometer (Sect. 2) to show the contrast gain when using two apertures instead of a single one (Sect. 3). We define the contrast gain map as the PSF ratio of a single aperture over a dual-aperture to highlight the gain zones (Sect. 3.1). We transpose this map as a function of the parallactic angle and of the radial distance from the axis to evaluate the exoplanet detection as a science case (Sect. 3.2). We study few limitations of the LBTI producing a contrast loss (Sect. 4). We estimate the sensitivity of the contrast gain to rotational blurring during the observations (Sect. 4.1), to chromatic effects for wide-band filters (Sect. 4.2) and to pistons and AO errors (Sect. 4.3). We finally discuss the reason why the LBTI can fundamentally provide a contrast gain compared to a telescope (Sect. 5).

2. POINT SPREAD FUNCTION OF TWO APERTURES *vs* ONE APERTURE

2.1 Theoretical point spread function

The Point Spread Function (PSF) is the image of an on-axis point object. The complex amplitude collected by the entrance aperture is propagated up to the focal plane of the instrument. The PSF equals to the square modulus of the Fourier transform of the complex amplitude at the entrance aperture (9). A single LBT provides a PSF which can be approximated to an Airy pattern, considering the relatively small obscuration.

The LBTI provides an "in-between" PSF, combining both diffractive and interferometric properties. The fringes appears within an Airy envelope, due to the double-aperture nature of the LBTI (Fig. 1). Knowing that the maximum baselength is $22.8m$ that is $22.8/8.4 \approx 3$ times larger than the sub-aperture diameter, about three bright fringes dominates within the Airy disk of an $8.4m$ sub-aperture, while faint fringes occur everywhere in the surrounding Airy rings. The theoretical PSF can be written as the product of a diffraction pattern and an interference pattern. The diffraction pattern is the sum of the two Airy functions delivered by each AO-equipped sub-aperture. The interference pattern is a fringe cosine function produced by both sub-apertures in the focal plane of the beam combiner. If all three patterns are centered at the same point anywhere in space, the PSF has a theoretical maximum (10).

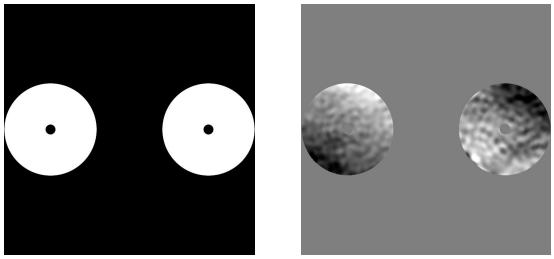

Figure 2. Complex amplitude of the entrance pupil of the LBTI made of two LBT apertures. Amplitude wavefront assuming a uniform illumination (left) and phase wavefront aberrations across the LBTI aperture (right).

Combining two sub-apertures instead of using a single one increases the maximum intensity in the PSF by a factor of four. First, the collected flux by the entrance aperture is doubled and the two Airy patterns are superimposed in the PSF. Second, the fringes produced within the Airy disc are intensified by a factor of two, by conservation of the energy which has been transferred from the - two - dark fringes into the - three - bright fringes. The PSF is normalised here so that the maximum of the central fringe equals to 1 for a diffraction-limited exposure and equals to the Strehl ratio for a seeing-limited exposure. Such normalisation does not account for the intensification by a factor 4, but allows to compare the focal pattern distribution in term of contrast provided by either one or two sub-apertures.

The longest baseline provides an angular resolution of $\lambda/B_{max} = 6.785mas$ (milli-arc-second) at $\lambda = 750nm$. At the opposite, the angular resolution is reduced to $\lambda/D = \lambda/8.4m$ in the direction perpendicular to the baseline and the PSF profile degenerates to the one of a single $8m$ sub-aperture (Fig. 1). The field of view of the LBTI interferometer is equal to the one provided by each AO system on each LBT.

2.2 Aberrated point spread function

The aberrated PSF can be viewed as the sum of a diffraction-limited core containing the coherent light (described above) and a speckle halo formed by incoherent light spread over a large and diffuse background. This speckle noise is essentially zero within the core, so that the fringe contrast of the LBTI is not affected. However, the surrounding fringes in the Airy rings are smoothed by such a halo. The PSF aberrations are directly related to the phase wavefront aberrations in the complex amplitude of the entrance pupil (Fig. 2).

The figures 3 and 4 show a comparison of the PSFs in the case of the LBT and the LBTI. The PSFs are computed by using 2 time series of residual wavefronts with an RMS of $\approx 100nm$ yielding an AO Strehl of 85% in H band (infrared) and 50% in R band (visible), according to the Maréchal approximation under good compensation conditions: $S_r = e^{-\sigma^2}$, where $\sigma = RMS \cdot 2\pi/\lambda$ is the residual AO wavefront variance. The AO Strehl S_r is directly related to the Root Mean Square (RMS) of the phase wavefront errors in the complex amplitude. Both LBT apertures provide almost the same performance with the same AO Strehl.

In the case of the LBTI interferometer, the interferometric Strehl (9) is defined as the ratio of the maximum of the aberrated PSF to the maximum of the unaberrated PSF. The interferometric Strehl is insensitive to a fringes displacement induced by a differential piston and remains valid out-of-axis, contrary to the traditional Strehl ratio which is not suitable in the case of an interferometer. Thus, the interferometric Strehl accounts for the fact that the high angular frequency information delivered by the interferometer is retained in the short exposure PSF despite a shift of the fringes.

The LBTI is highly sensitive to residual piston and AO errors, altering the PSF quality and thus reducing the interferometric Strehl (9). In presence of piston fluctuations, the loss of fringes contrast in a long exposure can be recovered by recording data cubes of short exposures so as to freeze the fringes and to avoid image blurring (9). However, as shown in this paper, the LBTI can offer unique properties for high contrast imaging if the residual pistons can be cophased in real time within a fraction of wavelength. For a piston larger than the limited coherence length (Sect. 4.2), the PSF turns into the superposition of the two Airy patterns, without fringes, reducing the maximum of the PSF by a factor of two compared to the theoretical one.

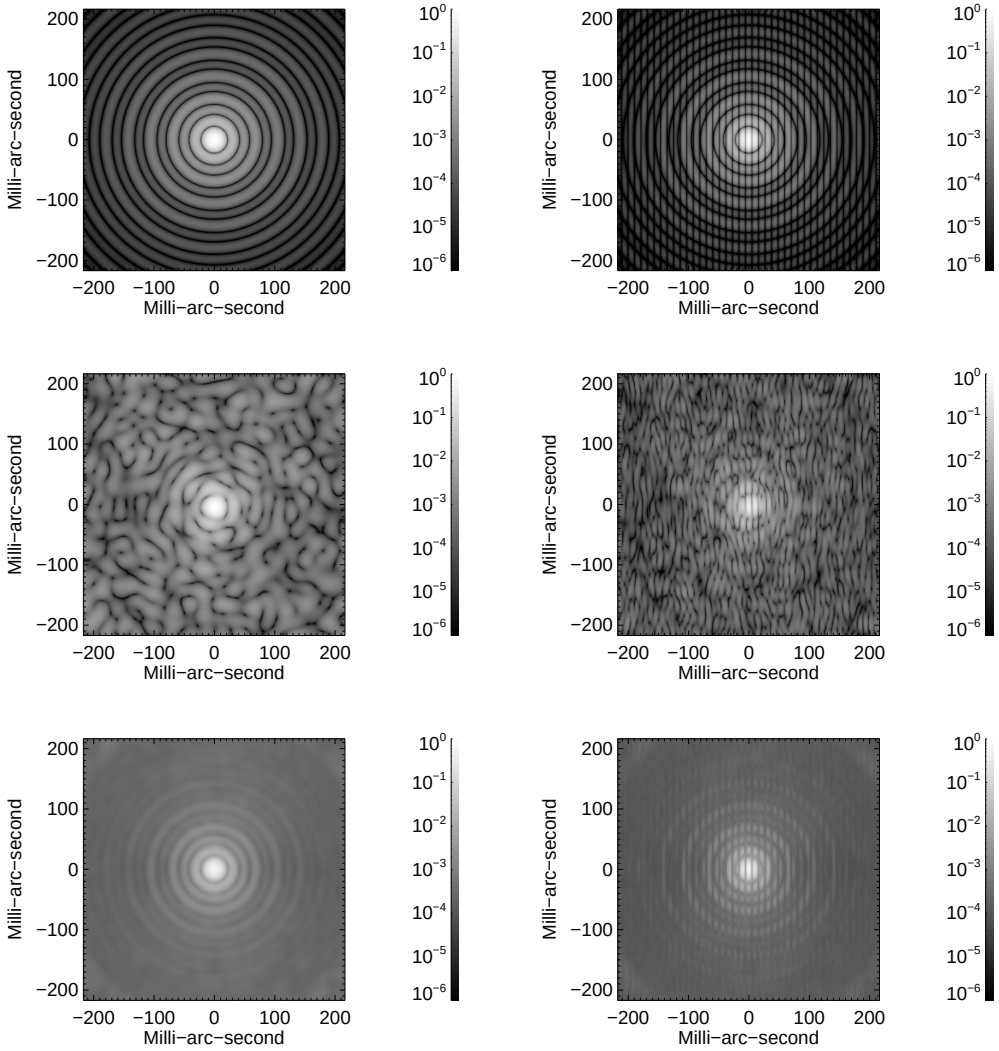

Figure 3. Point spread function of a single aperture with the LBT (left) and of two apertures with the LBTI (right). Diffraction-limited exposure (top), seeing-limited short exposure (middle) and seeing-limited long exposure (bottom). Logarithmic scale.

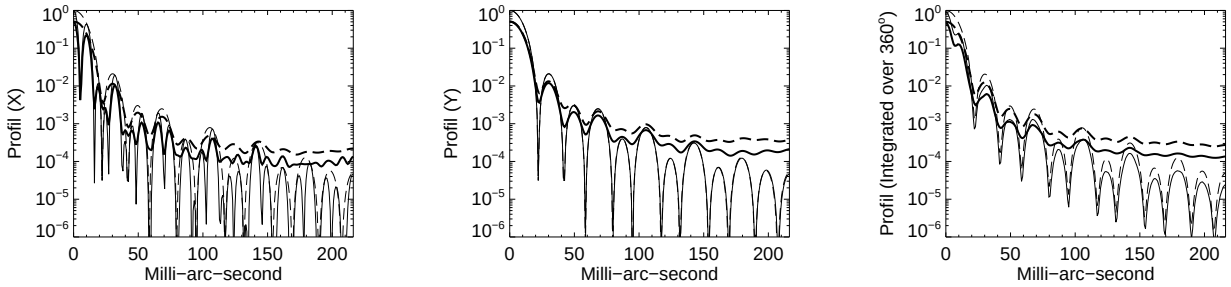

Figure 4. Point spread function profiles of two apertures with the LBTI (solid line) and of a single aperture with the LBT (dashed line). Diffraction-limited exposure (thin line) and seeing-limited long exposure (bold line).

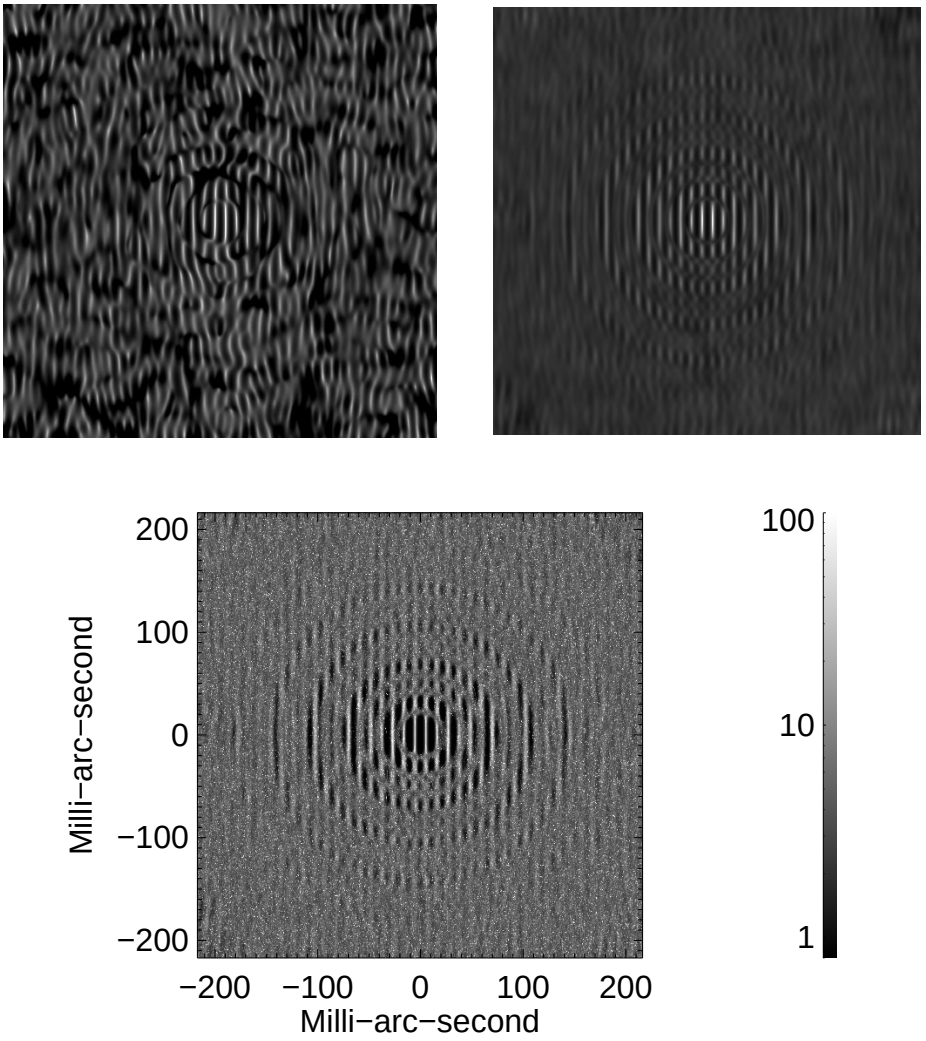

Figure 5. Contrast gain map of the LBTI *vs* the LBT. Ratio of a short exposure (top left), ratio of the long exposure G_{LE} (top right) and average of the ratio of the short exposures G_{SE} (bottom). Logarithmic scale.

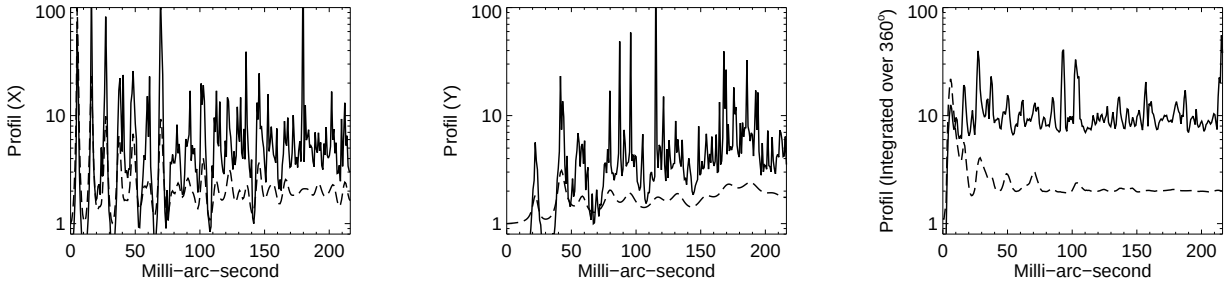

Figure 6. Contrast gain map profiles of the LBTI *vs* the LBT. Ratio G_{LE} of the long exposure (dashed line) and average of the ratio G_{SE} of the short exposures (solid line). The contrast gain averaged across the field equals to $G_{LE} \approx 2$ by using the long exposures and $G_{SE} \approx 10$ by using the short exposures.

The aberrations of the AO wavefronts (Fig. 2) disturb the interferometric PSF of the LBTI in a similiar way as they disturb the single aperture PSF (Fig. 3 and 4). The interferometric Strehl which can be achieved by the LBTI equipped with two FLAO is close to the AO Strehl provided by a FLAO standalone, as long as other sources of aberrations can be mitigated. The imaging performance of the LBTI is thus fundamentally limited by the AO-correction level. For a tip-tilt larger than the width of the Airy envelope, the decorrelations of the sub-PSFs destroys the interference pattern and the maximum PSF is reduced by a factor of four compared to the theoretical one.

Finally, the PSF of the LBTI can be optimised for high contrast imaging, providing a high Strehl regime (by each AO system) and a cophasing mode (by a fringe tracker inside the beam combiner) (9).

3. CONTRAST GAIN OF TWO APERTURES *vs* ONE APERTURE

3.1 Contrast gain map definition

We estimate next the contrast gain when using the LBTI made of two LBT sub-apertures instead of using a stand-alone LBT aperture. The contrast gain map is defined as the normalised ratio $G(x,y)$ of the PSF of a single LBT over the PSF of the LBTI. Using either one or the other LBT sub-aperture leads to close results, since both data sets have been generated with the same properties (identical phase power spectral density, RMS $\approx 100nm$).

$$G = \frac{PSF_{LBT}/PSF_{LBT\,Th.}(0)}{PSF_{LBTI}/PSF_{LBTI\,Th.}(0)} = \frac{PSF_{LBTI\,Th.}(0)}{PSF_{LBT\,Th.}(0)} \cdot \frac{PSF_{LBT}}{PSF_{LBTI}} = 4 \cdot \frac{PSF_{LBT}}{PSF_{LBTI}} \quad (1)$$

The contrast gain map uses the PSF normalised to the on-axis theoretical PSF value, so that the PSFs and the contrast gain is close to 1 on axis. The PSF of a single LBT aperture is multiplied by 4 with respect to the PSF of the LBTI aperture, accounting for the double flux and the fringe intensification (Sect. 2.1).

The figures 5 and 6 show the contrast gain map when using the LBTI in comparison with the stand-alone LBT. We distinguish the ratio of a short exposure, the ratio of the long exposure ($G_{LE}(x,y)$) and the average of the ratio of the short exposures ($G_{SE}(x,y)$). The contrast gain averaged across the field equals to $G_{LE} \approx 2$ and $G_{SE} \approx 10$ (according to the profile integrated over 360° in figure 6). Thus ,the global gain is improved by a factor 2 in contrast by using the long exposures and by a factor of 10 in contrast by using the short exposures. Indeed, fringes are still present in the short exposure, contrary to the long exposure where the fringes are blurred. Thus, there is some gain in grouping the short exposures with high gain. The contrast gain remains significant across the whole field of view for a short exposure and for the average of all the short exposures. At the contrary for a long exposure, the contrast gain is strongly attenuated far from the axis and remains efficient only in the fringes located in the Airy disk and in the first Airy rings (up to a radial distance of $\approx 100mas$ in this simulation).

In the contrast gain map (Fig. 5), dark means no gain and white means a gain of more than 100. The vertical white lines correspond to a gain of about 100 provided by the dark fringes (between the bright fringes). The grey circles correspond to a gain of about 10 provided by the LBTI in the dark Airy rings (between the bright Airy rings). A gain zone is produced in the valleys of the PSF formed by the dark rings and/or the dark fringes. An object (*e.g.* planet) is intensified if it is located in the dark fringes ($G \approx 10$ to 100) and/or in the dark rings ($G \approx 4$ to 20), while it remains unchanged in the white rings ($G \approx 1$). A huge contrast gain (few hundreds or thousands) in narrow zones (few *mas*) is achieved when both a dark fringe and a dark ring overlap. At the opposite, there is no gain in the three central bright fringes.

3.2 Contrast gain *vs* parallactic angle and radial distance

The Earth rotation allows to exploit various area in the contrast gain map where an object (*e.g.* a planet) will pass through several gain zones. This makes the LBTI well suitable for the Angular Differential Imaging (ADI) technique (11). The LBTI can offer a unique opportunity to search for extrasolar planets by adapting an ADI-like technique accounting for the contrast gain map distribution.

To estimate the sky coverage by contrast gain zones, a contrast gain map (Fig. 5) have been incrementally rotated around the central axis and added together (Fig. 7). Each incrementation is stored into a data cube,

providing the spatial coordinates (X,Y) and the parallactic angle (PA). By rotating and adding a layer perpendicular to the (X,Y) plan and passing through its centre along the PA axis in the data cube, another contrast gain map is generated as a function of the radial distance and the parallactic angle (Fig. 8). The contrast gain is plotted as a function of the parallactic angle, showing the contrast variation during the observation of a point-like object at a given radial distance (Fig. 9).

The purpose is to reproduce the detection of a planet by means of Earth rotation, like for the ADI technique. The field rotation (with a fixed pupil) enables to probe many areas in the field as a high contrast region where a planet can emerge from the background in the PSF. The gain in contrast evolves as a function of the rotation of a planet moving circularly around the center of the field (Fig. 9). A planet will be located either in a dark ring or in a white ring, depending on its radial distance. A planet will be alternatively located in a dark fringe and in a white fringe while the parallactic angle changes with Earth rotation. A planet close to the axis passes through few contrast gain zones of large width of few degrees. A planet far from the axis passes through many contrast gain zones of narrow width of about a degree.

A rotation of 15° is sufficient to pass through at least one contrast gain zone (Fig. 7). The fringe rotation is faster far from the axis, enabling a rapid and complete coverage of the contrast gain map (Fig. 7). At the contrary, for very small radial distance, the baseline projected onto the sky is slightly modified and the fringes rotates slowly close to the central axis. Increasing the observation time and the rotation angle is needed to probe several gain zones, especially if the planet is close to the central axis and/or is located in the alignment of the projected baseline.

An object aligned with the projected baseline corresponds to a useless part of the field of view without any contrast gain in the map integrated over 15° of rotation (Fig. 7). For an angular position along the baseline axis, the baseline projected in the object direction is reduced to the single aperture size and the resolution power is reduced by a factor $22.8/8.4 \approx 3$. The dark fringes disappear and the corresponding gain zones vanish as well in the baseline direction. This last restriction does not occur in practice for the LBTI, since the object is pointed by both telescopes at a time on an observed object generally close to their meridian.

Finally, the only restriction is to increase the whole observation time for objects at low zenith angles far from the LBTI rotation axis. Such constraint is mitigated by observing stars passing at their meridian, as requested for ADI. In addition, observing stars passing close to the zenith will maximise the rotation speed of the LBTI. Furthermore, the performance can be limited by other effects inherent to any interferometer equipped with AO systems or specific to the LBTI instrument.

4. CONTRAST LOSSES DUE TO LIMITATIONS OF THE LBTI

4.1 Contrast losses due to rotational blurring

Since the LBTI has an alt-azimuth mount, the sky will rotate with respect to the fringes during the observation. Indeed, the two primary mirrors remains horizontal while the fringes remains perpendicular to the horizon and fixed on the science detector. However, due to the Earth rotation, the sky rotates with respect to the entrance pupil, moving the stars on the detector, and thus producing images of star trails. The sky rotation can be compensated by a pupil rotation, by de-rotating the science detector in the LBTI. The entrance pupil (and the focal image) now rotates with respect to the sky which is fixed, causing rotational blurring of the fringes around the center of the science detector, and thus reducing the fringe contrast for a long exposure.

The rotational blurring of the PSF is negligible at small off-axis distance and does not affect the three central fringes. The rotational blurring is deleterious at larger radial distances, especially for very long integrations or observations near the zenith where the parallactic angle changes rapidly. In this study, we neglect such effect, assuming a set of short exposures ($\approx 1ms$) acquired in a short time (few minutes only). An integration time of 4 minutes - corresponding to a rotation of 1°- does not significantly alter the contrast gain map integrated over 1°(Fig. 7) compared to the map without any rotation (Fig. 5). Otherwise, above 2°(Fig. 7), the rotational blurring will mitigate the huge contrast gain in narrow zones, especially far from the axis, whereas the averaged contrast gain is maintained at the same level across the field. To prevent rotational blurring if a long integration time is need (above 10 minutes), post-treatment techniques may be applied on each individual frame, such as an adapted "shift-rotate-and-add" method.

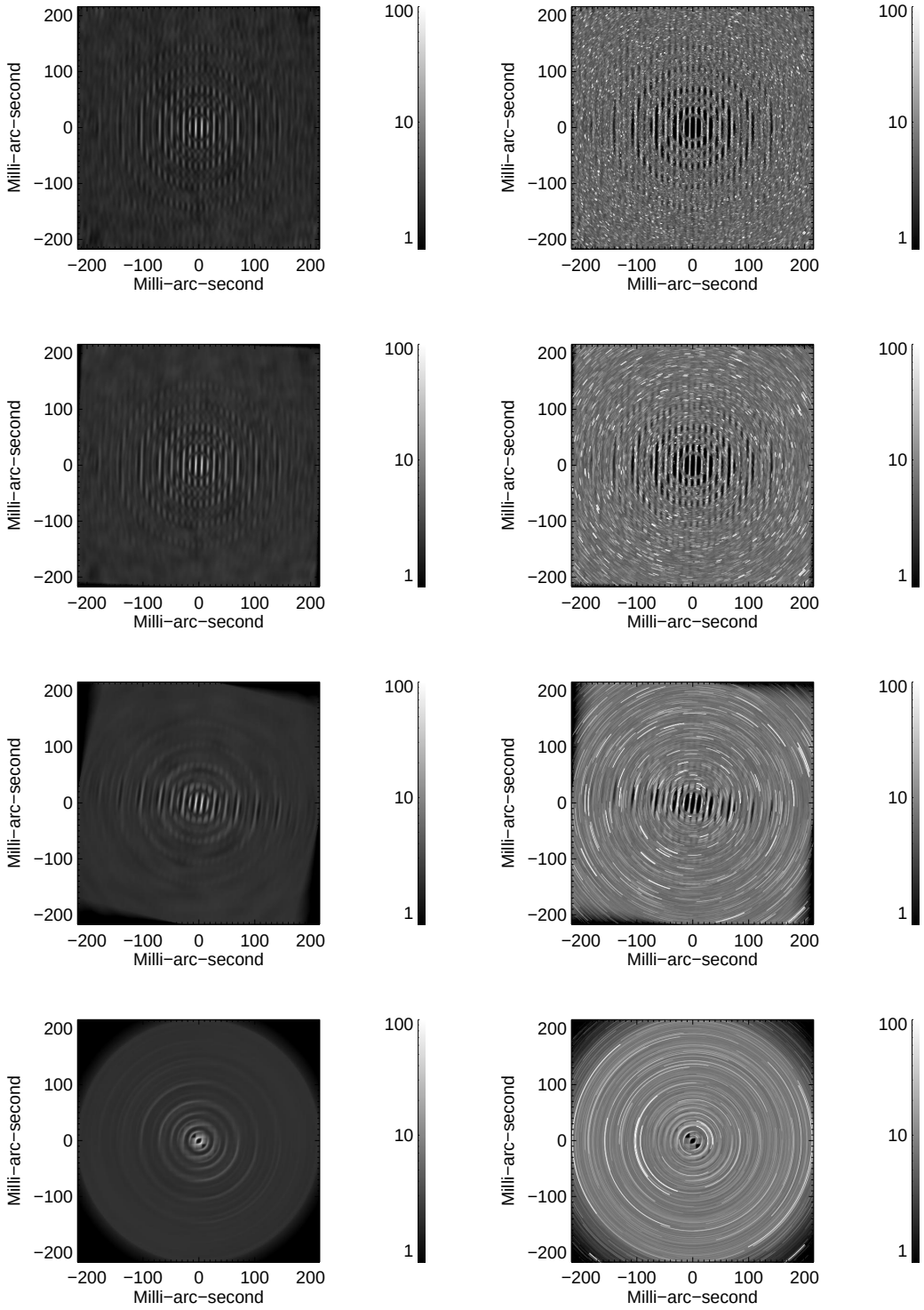

Figure 7. Integrated contrast gain map of the LBTI *vs* the LBT rotated over 1°, 2°, 15° and 90° (top to bottom). Ratio G_{LE} of the long exposure (left) and average of the ratio G_{SE} of the short exposures (right). Logarithmic scale.

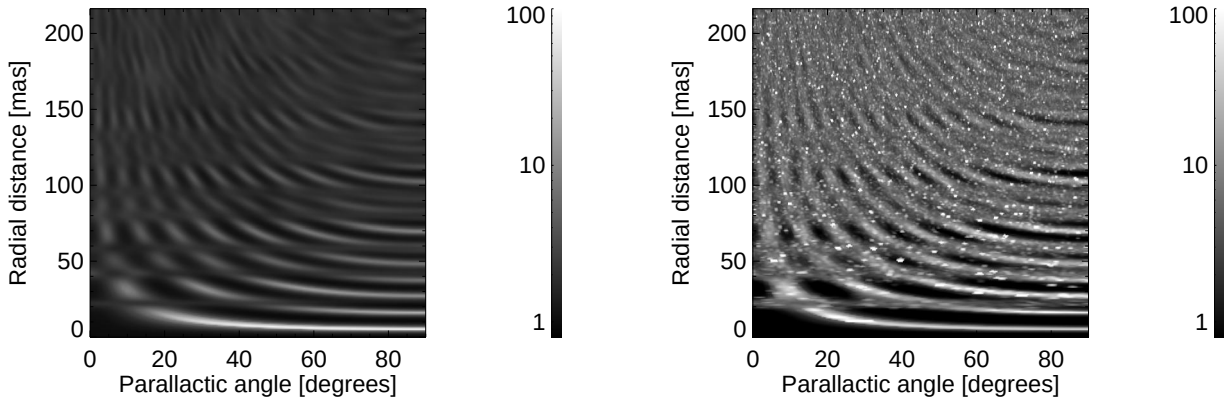

Figure 8. Contrast gain map of the LBTI *vs* the LBT as a function of the radial distance and the parallactic angle over 90°. Ratio G_{LE} of the long exposure (left) and average of the ratio G_{SE} of the short exposures (right). Logarithmic scale.

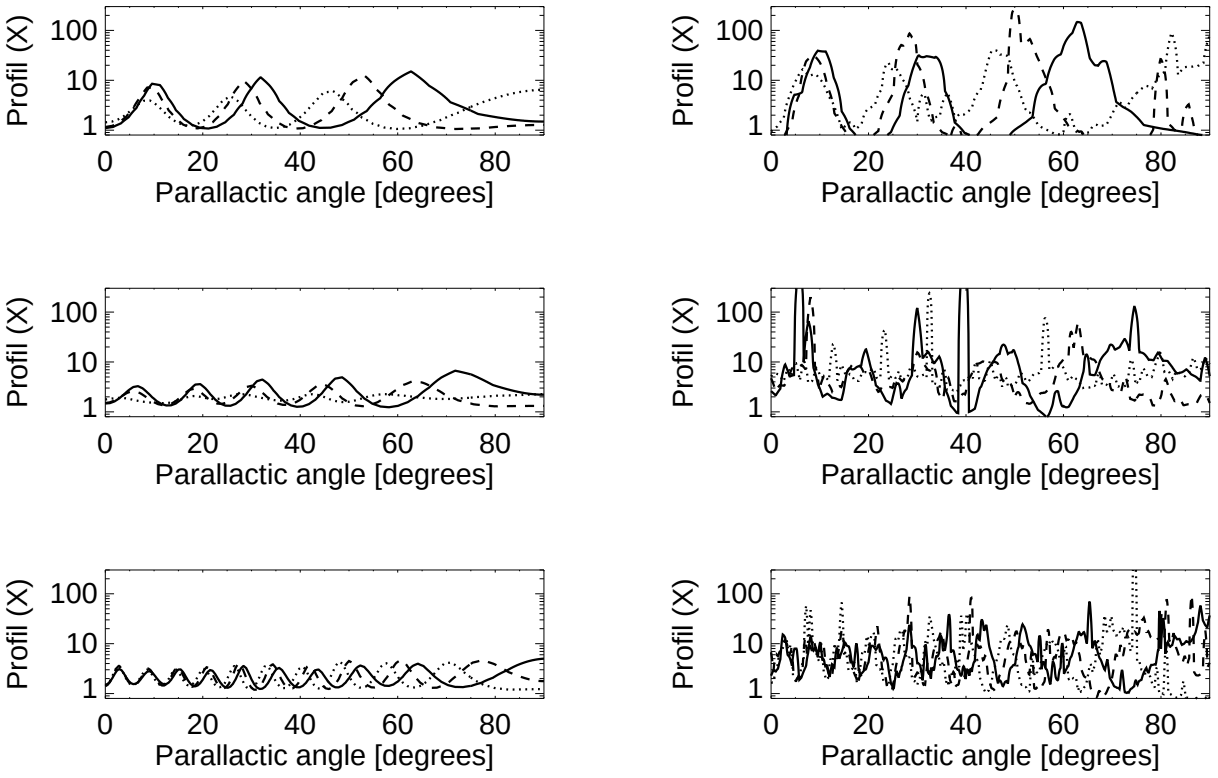

Figure 9. Contrast gain map profiles of the LBTI *vs* the LBT as a function of the parallactic angle over 90° for few given radial distances: $\approx 30mas$, $\approx 60mas$ and $\approx 120mas$ (top to bottom) from the central axis. Ratio G_{LE} of the long exposure (left) and average of the ratio G_{SE} of the short exposures (right).

The field rotation (no detector de-rotation) is generally recommended for high contrast imaging and exoplanet detection (*e.g.* ADI technique), preventing the effect of rotational blurring. The pupil and the image remains fixed for calibration purpose, while the sky rotates. A star (or planet) at a given radial distance describes in function of its parallactic angle a circular curve around the central axis of the PSF. In this study, assuming a perfect instrument free-of-aberration, the field and pupil rotations behave the same. Maintaining a fixed PSF (and a fixed contrast gain map) while moving the star along a circle is here equivalent to rotating the PSF (and rotating the contrast gain map) around its centre while considering the star at fixed position.

4.2 Contrast losses due to chromatic effects

For a given wavefront RMS in meter scale, the phase aberrations in the wavefront and the halo in the PSF are more intense in the visible than in the infrared. For example, an RMS of $\approx 100nm$ yields to an AO Strehl of 85% in H band (infrared) and 50% in R band (visible). These simulations show the most critical case, when the image is significantly distorted in the visible wavelengths.

The interference pattern is limited in extent by the coherence length. The coherence length l_c of the light is related to the spectral filter bandwidth $\Delta\lambda$ via $l_c = \lambda^2/2\Delta\lambda$. The light can interfere in the focal plane even for large pistons values, providing a large coherence length (longer wavelength, smaller filter bandwidth).

The field of view in the PSF is wavelength-dependant. Both the diffraction and interference functions vary as a function of the wavelength. The chromatic effects are deleterious for wide spectral bandwidths. Wide-band filters produce a smearing of the image pattern across the field of view which is more drastic far from the axis. The PSF at a given wavelength fills the valleys of the PSF at another wavelength. The sum of the monochromatic PSFs yields a smoothed halo destroying the thin structures in the image pattern. For wide-band filters, the contrast gain map is smoothed to a quasi-constant contrast gain across the field of view. Consequently, the contrast gain depends neither on the parallactic angle, nor on the radial distance and becomes homogeneous, except in its central part. Wide-band filters enable to cancel the restrictions of rotation to probe various gain zones, yielding to the same method of detection as the classical ADI technique (11). However, faint planets are not accessible for wide bandwidths.

Narrow-band filters are mandatory to achieve a huge contrast gain in narrow zones where a dark fringe and a dark ring overlap. Using a narrow band filter (spectral bandwidth $\Delta\lambda < 10\%\,\lambda$) will not significantly affect the PSF quality (12). The central part of the PSF remains unchanged, while the edge of the field is smoothed by chromatic effects.

4.3 Contrast losses due to pistons and AO errors

Differential pistons and AO wavefront (tip-tilt) errors affect the contrast of the fringe pattern and of the Airy patterns in the PSF of the LBTI (9). The contrast gain achievable by the LBTI is fundamentally limited by the AO-correction level (Sect. 2.2). The light scattered by AO aberrations blur the image and tends to fill the valleys by altering both the dark fringes and rings. However, a snapshot image retains the fringes formed in a halo of speckles (Fig. 3), enabling speckle imaging (13). We argue in this paper that the speckle halo contains not only high angular resolution information but also high contrast imaging information, providing a good compensation by AO systems.

Piston fluctuations attenuate the fringes contrast in a long exposure by smoothing the dark fringes while preserving the dark rings (9). The contrast gain map of the long exposure is attenuated by piston errors of RMS above a fraction of ten of wavelength (Fig. 10). While the averaged gain G_{LE} is close to 1.5 for pistons RMS $\approx \lambda/4$, the gain is definitively lost for pistons RMS above $\approx \lambda/2$.

At the opposite, a piston preserves the fringes contrast in a short exposure without altering neither the dark fringes nor the dark rings (9). Piston fluctuations induce a random shift of the fringes and, as well, a random shift of the contrast gain zones, enlarging their sizes and attenuating their maximum gains (Fig. 10). The contrast gain map of the average of the ratio G_{SE} of the short exposures is smoothed by large piston errors, but the average gain across the field is maintained to $G_{SE} \approx 10$. A huge contrast gain in narrow zones is only achieved by means of a cophasing mode reducing the piston RMS to a fraction of ten - or more - of wavelength.

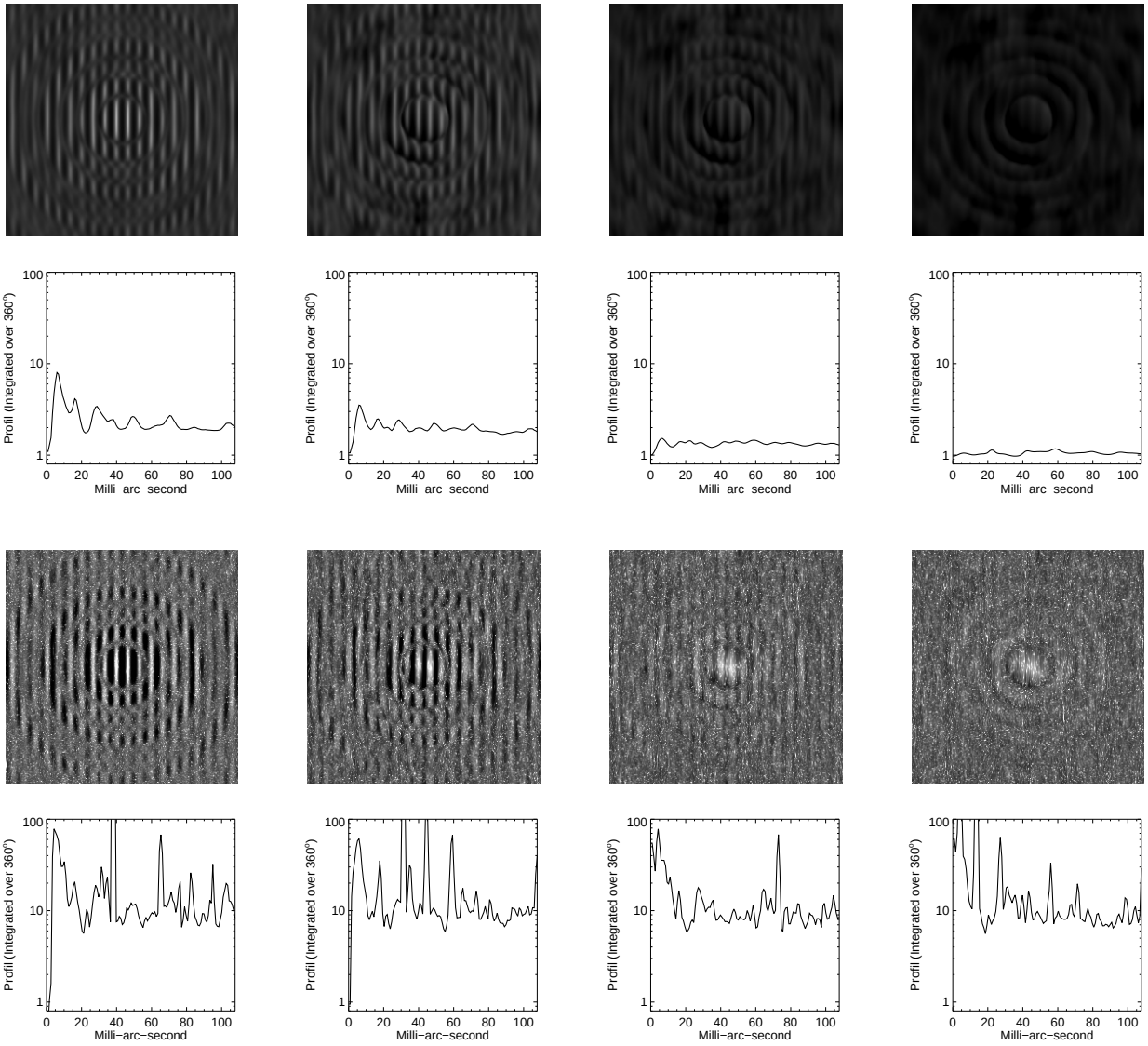

Figure 10. Contrast gain map with AO errors of RMS $\approx \lambda/8 \approx 100nm$ and with piston errors of RMS $\approx \lambda/16, \lambda/8, \lambda/4, \lambda/2$ (left to right). Ratio G_{LE} of the long exposure (top) and average of the ratio G_{SE} of the short exposures (bottom). Same scale for the distribution as in fig. 5.

In addition, a piston induces a shift of the fringes with respects to the rings which can create locally in a short exposure a huge contrast gain when a dark fringe and a dark ring overlap. The highly contrasted zones induced by random pistons may be helpful for high contrast imaging applications (*e.g.* lucky imaging) by selecting the frames for which such huge local gain occurs onto the faint planet.

5. DISCUSSION

Numerical simulations for the LBTI have shown a significant gain in contrast when using two $8m$ AO telescopes instead of one in a high Strehl and cophased regime (assuming an AO-corrected wavefront RMS and a residual cophased piston RMS below a fraction of wavelength). We argue that the LBTI can fundamentally provide

a contrast gain compared to homologous telescopes made of a single aperture, by properly combining the two separated wavefronts from each sub-aperture. The LBTI can provide in the visible wavelengths not only high angular resolution ($\approx 6.5mas$ at $750nm$) and high sensitivity (by a factor 4), but also a gain in contrast (by a factor 10 to 100) compared to the stand-alone adaptive optics used on each LBT aperture. Two coupled AO systems outperform a stand-alone AO system in terms of contrast by improving the spatial coherence, but not the temporal one. The contrast gain will be significant assuming bright guide stars and good atmospheric conditions.

The Fizeau focus acts as a natural spatial filter or, equivalently, as an angular frequency sampler. The LBTI aperture may be compared with the Young experiment, where a single spatial/angular frequency is sampled by two small sub-apertures forming one baseline. Similarly, the sparse aperture masking technique (14), using a mask with holes across the aperture of a single telescope, enables to probe a finite number of spatial/angular frequency samples with various base lengths and base orientations. The LBTI has large $8m$ sub-apertures with respect to the $14m$ baseline, probing numerous frequency samples mainly in one direction.

The LBTI has a resolution power of a $23m$ telescope in one direction only. The contrast of the LBTI is affected by aberrations in one direction only, whereas the contrast of a $23m$ telescope is affected by the aberrations in all the directions within the $23m$ entrance pupil. Therefore, the contrast loss produced by the aberrations of a $23m$ telescope in all the directions is reduced to the contribution of two $8m$ telescopes in one main direction while preserving the resolution power in this direction. Indeed, the incoherent light induced by aberrations outside of the two $8m$ sub-apertures but inside a large $23m$ telescope are purely removed, as well as the corresponding light scattered into the halo in the PSF. At the contrary, the coherent light corrected from the turbulence by AO across each sub-aperture (except the piston) contributes directly to the PSF pattern, producing a contrast gain by encoding only the useful information in one main direction. In other words, instead of probing the whole pupil providing in real-time a centro-symmetric PSF, a contrast gain is achievable by sampling the pupil in one direction only while recovering the centro-symmetry of the PSF by Earth rotation.

6. CONCLUSION

The fundamental contrast gain shown in this paper may justify the development of a high contrast imaging mode in the infrared wavelengths at the LBTI and, in particular, in the visible wavelengths with the LIVE project. Indeed, the visible PSF contains thinner structures than the infrared PSF, providing more valleys where planets can be detected. The interferometric and diffractive PSF in the visible produces about 10 times more Airy rings and interferometric fringes than in the infrared. Therefore, a visible mode of observation at the LBTI could provide not only the largest angular resolution but also the highest contrast gain never achieved up to now by the current class of $8m$ telescopes.

Other projects would take benefit from this fundamental contrast gain. A new mode of observation could be proposed on the GMT by only using two segments at a time and by alternatively changing the baselines provided by the 7 segments. This mode provides few PSFs with various orientations and performs a better contrast than the one of the classical mode using simultaneously all the segments of the GMT.

Finally, the original optical concepts of the LBTI and the GMT can provide huge contrast imaging capabilities. The LBTI and the GMT may reach unprecedented performance in angular resolution, in sensitivity and in high contrast imaging on a large field of view, assuming efficient adaptive optics, tip-tilt correctors and cophasing systems. This paper enables to promote the AO interferometers as powerful instruments for future challenging projects, in particular for extrasolar planet detection.

References

[1] Hill, J. M., Ashby, D. S., Brynnel, J. G., Christou, J. C., Little, J. K., Summers, D. M., Veillet, C., and Wagner, R. M., "The Large Binocular Telescope: binocular all the time," in [*Ground-based and Airborne Telescopes V*], *Proc. SPIE* **9145**, 914502 (July 2014).

[2] Hinz, P., Bailey, V. P., Defrère, D., Downey, E., Esposito, S., Hill, J., Hoffmann, W. F., Leisenring, J., Montoya, M., McMahon, T., Puglisi, A., Skemer, A., Skrutskie, M., Vaitheeswaran, V., and Vaz, A., "Commissioning the LBTI for use as a nulling interferometer and coherent imager," in [*Optical and Infrared Interferometry IV*], *Proc. SPIE* **9146**, 91460T (July 2014).

[3] Esposito, S., Riccardi, A., Fini, L., Puglisi, A. T., Pinna, E., Xompero, M., Briguglio, R., Quirós-Pacheco, F., Stefanini, P., Guerra, J. C., Busoni, L., Tozzi, A., Pieralli, F., Agapito, G., Brusa-Zappellini, G., Demers, R., Brynnel, J., Arcidiacono, C., and Salinari, P., "First light AO (FLAO) system for LBT: final integration, acceptance test in Europe, and preliminary on-sky commissioning results," in [*Proc. SPIE*], *Proc. SPIE* **7736**, 9 (July 2010).

[4] Hinz, P., Arbo, P., Bailey, V., Connors, T., Durney, O., Esposito, S., Hoffmann, W., Jones, T., Leisenring, J., Montoya, M., Nash, M., Nelson, M., McMahon, T., Pinna, E., Puglisi, A., Skemer, A., Skrutskie, M., and Vaitheeswaran, V., "First AO-corrected interferometry with LBTI: steps towards routine coherent imaging observations," in [*Optical and Infrared Interferometry III*], *Proc. SPIE* **8445**, 84450U (July 2012).

[5] Leisenring, J. M., Skrutskie, M. F., Hinz, P. M., Skemer, A., Bailey, V., Eisner, J., Garnavich, P., Hoffmann, W. F., Jones, T., Kenworthy, M., Kuzmenko, P., Meyer, M., Nelson, M., Rodigas, T. J., Wilson, J. C., and Vaitheeswaran, V., "On-sky operations and performance of LMIRcam at the Large Binocular Telescope," in [*Ground-based and Airborne Instrumentation for Astronomy IV*], *Proc. SPIE* **8446**, 84464F (Sept. 2012).

[6] Defrère, D., Hinz, P., Downey, E., Ashby, D., Bailey, V., Brusa, G., Christou, J., Danchi, W. C., Grenz, P., Hill, J. M., Hoffmann, W. F., Leisenring, J., Lozi, J., McMahon, T., Mennesson, B., Millan-Gabet, R., Montoya, M., Powell, K., Skemer, A., Vaitheeswaran, V., Vaz, A., and Veillet, C., "Co-phasing the Large Binocular Telescope: status and performance of LBTI/PHASECam," in [*Optical and Infrared Interferometry IV*], *Proc. SPIE* **9146**, 914609 (July 2014).

[7] Herbst, T. M., Ragazzoni, R., Eckart, A., and Weigelt, G., "LINC-NIRVANA: the Fizeau interferometer for the Large Binocular Telescope," in [*Optical and Infrared Interferometry*], *Proc. SPIE* **7013**, 701326 (July 2008).

[8] Hinz, P., Esposito, S., Apai, D., Brusa, G., Close, L., Guyon, O., Hill, J., Males, J., Pinna, E., and Puglisi, A., "Toward visible wavelength coherent imaging with the LBT," in [*Optical and Infrared Interferometry IV*], *Proc. SPIE* **9146**, 914605 (July 2014).

[9] Patru, F., Puglisi, A., Riccardi, A., Pinna, E., Arcidiacono, C., Hill, J., and Hinz, P., "Sensitivity to differential piston and to adaptive optic errors with the Large Binocular Telescope Interferometer," in [*This proceeding*], *Proc. SPIE* (2016).

[10] McCarthy, D. W., Sabatke, E. M., Sarlot, R. J., Hinz, P. M., and Burge, J. H., "Cryogenic beam-combiner for very low background 2- to 20-um interferometry on the 22.8-m Large Binocular Telescope," in [*Interferometry in Optical Astronomy*], Léna, P. and Quirrenbach, A., eds., *Proc. SPIE* **4006**, 659–672 (July 2000).

[11] Marois, C., Lafrenière, D., Doyon, R., Macintosh, B., and Nadeau, D., "Angular Differential Imaging: A Powerful High-Contrast Imaging Technique," *Astrophysical Journal* **641**, 556–564 (Apr. 2006).

[12] Straubmeier, C., Bertram, T., Eckart, A., Wang, Y., Zealouk, L., Herbst, T. M., Andersen, D. R., Ragazzoni, R., and Weigelt, G. P., "The fringe and flexure tracking system for LINC-NIRVANA: basic design and principle of operation," in [*New Frontiers in Stellar Interferometry*], Traub, W. A., ed., *Proc. SPIE* **5491**, 1486 (Oct. 2004).

[13] Labeyrie, A., "Attainment of Diffraction Limited Resolution in Large Telescopes by Fourier Analysing Speckle Patterns in Star Images," *Astronomy and Astrophysics* **6**, 85 (May 1970).

[14] Lacour, S., Tuthill, P., Amico, P., Ireland, M., Ehrenreich, D., Huelamo, N., and Lagrange, A.-M., "Sparse aperture masking at the VLT. I. Faint companion detection limits for the two debris disk stars HD 92945 and HD 141569," *Astronomy and Astrophysics* **532**, A72+ (2011).